Sustainable Structures
ISSN: 2789-3111 (Print); ISSN: 2789-312X (Online)
http://www.sustain-dpl.com/journal/sust
DOI: 10.54113/j.sust.2024.000059

ORIGINAL ARTICLE

Behaviour and design of extruded high-strength aluminium alloy SHS beam-columns

Beibei Li [a,b,c,d], Pengcheng He [a*], Jingfeng Wang [a,b,c,d], Yuanqing Wang [e]

[a] School of Civil Engineering, Hefei University of Technology, Hefei, 230009, China
[b] Anhui Key Laboratory of Civil Engineering Structures and Materials, Hefei University of Technology, Hefei 230009, China
[c] Anhui Advanced Steel Structure Technology and Industrialization Collaborative Innovation Center, Hefei, 230009, China
[d] Engineering Research Center of Low-carbon Technology and Equipment for Cement-based Materials, Ministry Education, Hefei, 230009, China
[e] Department of Civil Engineering, Tsinghua University, Beijing, 100084, China
[*]Corresponding Author: Pengcheng He. Email: pengchenghe2023@163.com.

Abstract: An extensive study of beam-columns made from 7A04-T6 aluminum alloy in a square hollow section (SHS) configuration is presented in this paper, integrating both experimental and numerical work to study their flexural buckling behaviour. Eight pin-ended SHS specimens with two extruded SHS profiles - 80 ×5 and 120 × 10 (in mm), were tested under eccentric compression, along with tests of material coupons and measurements of initial geometric imperfections. The experimental data were employed in the investigation to assess the validity of the numerical model, which was subsequently subjected to a series of parametric analyses aimed at expanding the existing results across a wider spectrum of slenderness ratios, cross-section dimensions, and load combinations. Both experimental and simulated datasets were employed to verify the precision of resistance forecasts for SHS beam-columns by design approaches outlined in European, Chinese and American standards. Findings indicated that both the European and Chinese standards tended to provide relatively conservative predictions for buckling resistances, while the American standard sometimes produced predictions leading to higher risk. Finally, a modification strategy for the design of AA7A04-T6 SHS beam-columns, utilizing modified interaction buckling factors that account for non-dimensional member slenderness and compression resistances, was suggested to enhance the precision and reliability of resistance forecasts.

Keywords: Eccentric compression; 7A04-T6 high-strength aluminium alloy; interaction equation; buckling resistances; modification strategies

1 Introduction

Aluminium alloy (AA) has been extensively utilised in industrial, building, bridge and marine construction, due to its excellent specific strength, outstanding corrosion resistance, elegant appearance and the flexible extrusion [1-3]. In recent decades, investigations into the performance of AA members have principally concentrated on normal-strength aluminium alloys, with various aspects of structural

Received: 12 June 2024; Received in revised form: 12 August 2024; Accepted: 30 October 2024

performance across different cross sections. Specifically, a lot of research on the structural behavior of AA members subjected to axial force has been carried out, including the AA6061-T6 and AA6063-T5 SHS, rectangular hollow section (RHS), I-type and L-type members by Su et al. [4], Wang et al. [5] and Zhang et al. [6], as well as the AA6082-T6 RHS, circular hollow section (CHS) and I-type section members in Adeoti et al. [7] and Wang et al. [8]. Meanwhile, bending performance of AA beams was widely assessed, including the AA6082-T6 and AA6082-T4 SHS, RHS, and I-type members under moment gradient in Moen et al. [9], AA6061-T6 and AA6063-T5 SHS, RHS and complex typed members under pure bending moments by Zhu and Young [10], Su et al. [11] and Kim and Pekö z [12], and AA6061-T6 and AA6063-T5 perforated and unperforated SHS and RHS beams under gradient and pure bending moments in Feng et al. [13]. Furthermore, the structural response of AA beam-columns was also investigated, encompassing AA6061-T6 CHS and double-layer I-type section beam-columns in Zhu and Young [14] and Du et al. [15], and AA6082-T6 SHS, CHS, and L-type section beam-columns in Zhao et al. [16-17], as well as AA6082-T6 I-type section perforated members in Kong et al. [18]. Previous literature reveals that the stability behaviour of AA members can be well predicted by various prediction methodologies, for instance, direct strength method [19] and continuous strength method [20], which helped to popularize AA in the construction engineering field.

However, most current standards, including the European specification (EN 1999-1-1:2007) [21], Chinese specification (GB 50429-2007) [22], and American specification (AADM-2020) [23], just cover design methods for the normal-strength AA with 0.2% proof strength ($\sigma_{0.2}$) less than 300 MPa. With the high-rise structures advancing rapidly, architects and designers have shifted their interest to high-strength aluminium alloys for their superior mechanical properties, due to their substantial potential for bearing heavier loads using reduced cross-section dimensions. Existing studies have shown significant differences in material characteristics between high-strength and normal-strength AAs, which inevitably affect the behavior of high-strength AA at both the component and structural levels [2]. The 7××× series AA, recognized for their high strength with a yield strength surpassing 500 MPa, are hailed as key materials in aerospace applications. Despite this, their use in construction remains restricted by the lack of reliable design standards. Recently, the mechanical characteristics of 7××× series AA have been explored by several scholars. Specifically, Wan et al. [24] investigated the dynamic response of AA7A04 at high strain rates by employing a Kolsky bar test. Quan and Alderliesten [25] clarified the fatigue crack growth of AA7075-T6 via an experimental study. Wang et al. [26] and Yun et al. [27] undertook calibrations for the cyclic and monotonic constitutive relationship of AA7A04. Rong et al [28] and Li et al [29-30] conducted axial loading tests on AA7A04-T6 SHS and CHS members, resulting in new buckling curves to refine the predictions for column resistances. Yuan et al. [31] investigated the flexural buckling performance of AA7075-T6 I-type members under axial force and proposed a new column curve. Hu et al. [32] and Rong et al. [33] evaluated the stability performance of AA7A04-T6 beam-columns through experiments and numerical simulations, revealing that most of current standards tended to underestimate the resistance of the high-strength AA. However, there have still been limited investigations into the structural behaviour and design methods for 7××× series AA, especially the stability performance and reliable forecasting methods for AA7A04-T6 under eccentric compression.

Therefore, eight pin-ended AA7A04-T6 SHS members were assessed under eccentric loading during this research. The reliable finite element (FE) model was developed by comparing experimental outcomes. In succession, comprehensive parametric analyses were conducted, including the geometric parameter and the loading condition. The experimental findings and simulation analysis were checked against the forecasted resistances using the existing AA design criteria, including EN 1999-1-1:2007 [21], GB 50429-2007 [22], and AADM-2020 [23], to evaluate their accuracy. Finally, a novel design approach was proposed to enhance the precision and reliability of buckling carrying capacity predictions based on the framework of existing standards for AA7A04-T6 SHS beam-columns.

2 Experimental investigations

2.1 General

Eight AA7A04-T6 extruded SHS members were subjected to eccentric compression testing at room temperature to explore their flexural buckling responses and resistances. The nominal sizes of the SHS are 80×80×5 mm and 120×120×10 mm, which are categorized as Class 2-3 sections given in EN 1999-1-1:2007 [21]. With each nominal size, four beam-columns with various lengths were tested. The surveyed geometric parameters are tabulated within **Table 1**, as per the labelling convention depicted in **Fig. 1**, where L represents the member length; L_e represents the considered member length (i.e., the spacing between pinned end knife edges), with $L_e = L+124$ mm. The slenderness ratio, λ, is calculated as L_e/i_c and the non-dimensional slenderness, $\bar{\lambda}_g$, is calculated as $\bar{\lambda}_g = [(\sigma_{0.2}A_g)/N_{cr}]^{0.5}$, in which A_g represents the gross cross-section area. Additionally, N_{cr} denotes the Euler buckling force, and $N_{cr} = \pi^2 EI/L_e$. All specimens were labelled according to the illustration in **Fig. 2**.

Table 1. Summary of dimensions of SHS beam-columns

Specimen	B (mm)	H (mm)	t (mm)	A_g (mm^2)	L (mm)	L_e (mm)	λ	$\bar{\lambda}_g$
SHS-80-47-E21	80.08	80.15	5.00	1438.62	1300.4	1424.40	46.98	1.28
SHS-80-60-E24	79.92	80.07	4.96	1425.44	1699.7	1823.70	60.23	1.64
SHS-80-77-E24	79.85	79.90	4.93	1415.23	2200.0	2324.00	76.85	2.09
SHS-80-91-E19	80.03	80.13	4.94	1421.92	2649.8	2773.80	91.48	2.49
SHS-120-41-E28	120.35	120.29	10.18	4220.06	1699.7	1823.70	41.24	1.12
SHS-120-51-E29	120.34	120.37	10.02	4163.47	2148.9	2272.90	51.31	1.40
SHS-120-62-E29	120.29	120.27	10.22	4230.28	2600.8	2724.80	61.69	1.68
SHS-120-77-E32	120.50	120.35	10.23	4239.47	3298.0	3422.00	77.38	2.10

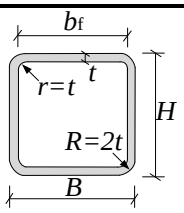

Fig. 1. Diagram of the cross-sectional geometry.

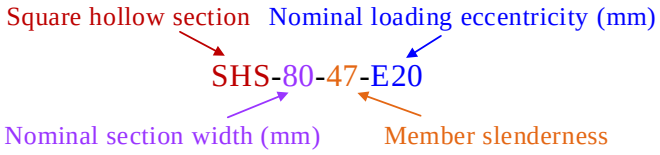

Fig. 2. Labelling convention for test specimens.

2.2 Material properties

To understand the full range of mechanical behaviour and key characteristic parameters of AA7A04-T6, three repeated tensile coupons from each profile, as indicated by **Fig. 3** and **Table 2**, were tested. The stress-strain behaviour of the 5-mm and 10-mm thick AA7A04-T6 coupons is illustrated in **Fig. 4**.

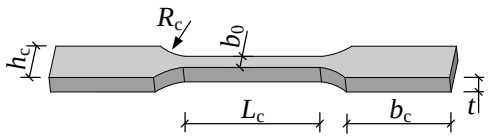

Fig. 3. Schematic diagram of coupons.

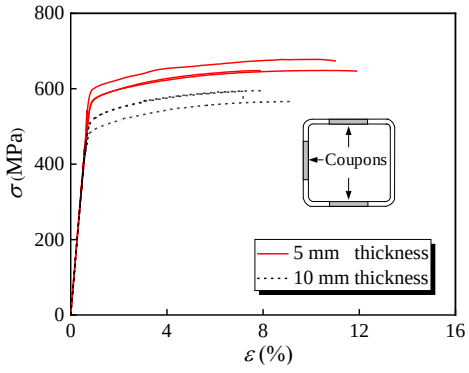

Fig. 4. Surveyed stress-strain curves.

Meanwhile, the Young's modulus (E), the yield strength ($\sigma_{0.2}$), the ultimate strength (σ_u), the corresponding strain at σ_u (ε_u) and the strain hardening exponent of Ramberg-Osgood function (n) are listed

in **Table 2**. Notably, $n = \ln(0.002/\varepsilon_{0,u})/\ln(\sigma_{0.2}/\sigma_u)$ [21], where $\varepsilon_{0,u}=\varepsilon_u-0.002$. Significantly, the mechanical characteristics of the extruded AA are similar across all regions [19].

Table 2. Material properties

Section ($B\times H\times t$)	t (mm)	b_0 (mm)	L_c (mm)	R_c (mm)	b_c (mm)	h_c (mm)	E (GPa)	$\sigma_{0.2}$ (MPa)	σ_u (MPa)	ε_u (%)	n
80×80×5mm	4.83	14.94	80	30	60	45	75.43	581.0	658.6	9.41	30.6
120×120×10mm	10.05	24.94	120	40	40	50	73.70	507.5	584.8	8.00	25.8
Mean							74.57	544.3	621.5	8.87	28.2
COV							0.018	0.072	0.063	0.142	0.09

2.3 Initial imperfections

Geometric imperfections as well as residual stresses necessarily become inherent in SHS members during manufacturing procedure of the members. Nevertheless, the residual stresses of aluminium alloy members produced through extrusion-forming technology typically remains around 20 MPa and therefore can be negligible [17]. Considering that the buckling onset and eccentric compression resistances of aluminium alloy members were affected by imperfections, the initial global imperfections were appraised. The methodology employed for measurements is depicted in **Fig. 5**, which aligned with that of previous research [29] conducted on aluminium alloy members.

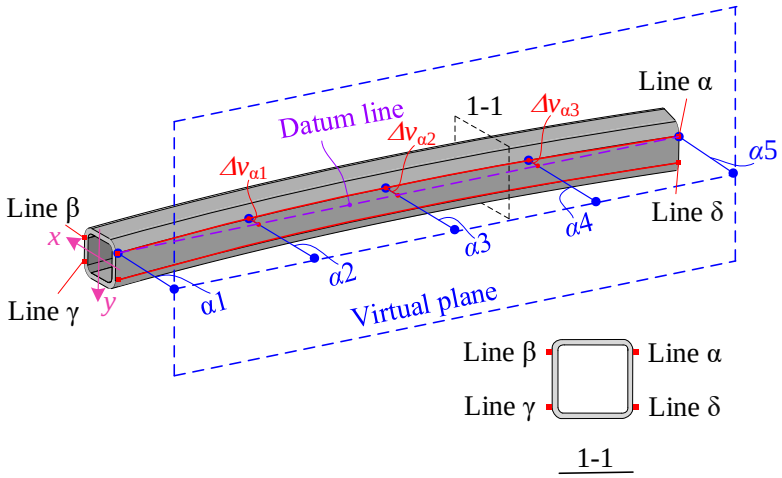

Fig. 5. Geometric imperfection measurement schematic.

Table 3. Surveyed global geometric imperfections and member load eccentricities

Specimen	e_0 (mm)	Δw_g (mm)	$\Delta w_g/L$ (‰)
SHS-80-47-E21	20.4	0.91	0.70
SHS-80-60-E24	22.5	1.15	0.68
SHS-80-77-E24	22.6	1.55	0.71
SHS-80-91-E19	17.0	2.18	0.82
SHS-120-41-E28	27.0	1.32	0.78
SHS-120-51-E29	27.1	1.71	0.80
SHS-120-62-E29	27.7	1.43	0.55
SHS-120-77-E32	29.9	1.66	0.50

The initial global geometric imperfections along each member length were determined utilizing a total station and callipers. A total station was mounted on one side of the fixed specimen, slightly offset from its longitudinal centreline. Measurements were taken using a vernier gauge to determine the variation (α_1 - α_5) at the end and quartile points throughout each lengthwise line of the specimen (α, β, γ and δ) against a

virtual plane established by the total station. Geometric relationships can be employed to assess the alignment of the longitudinal edge lines with respect to the datum line, which is determined by two measured points at the ends of the specimen ($\Delta v_{\alpha 1}$, $\Delta v_{\alpha 2}$ and $\Delta v_{\alpha 3}$). The maximum of Δv_1, Δv_2 and Δv_3 were determined, constituting the global geometric imperfection amplitudes (Δw_g), as reflected by **Table 3**, hereinto $\Delta v_1 = (\Delta v_{\alpha 1}+\Delta v_{\beta 1}+\Delta v_{\gamma 1}+\Delta v_{\delta 1})/4$, $\Delta v_2 = (\Delta v_{\alpha 2}+\Delta v_{\beta 2}+\Delta v_{\gamma 2}+\Delta v_{\delta 2})/4$ and $\Delta v_3 = (\Delta v_{\alpha 3}+\Delta v_{\beta 3}+\Delta v_{\gamma 3}+\Delta v_{\delta 3})/4$. Clearly, the global geometric imperfections of all members ranged from 0.5 to 0.82 times the $0.001L$, which were remained below $0.001L$.

2.4 Eccentric compression tests

To examine the beam-column buckling performance and buckling carrying capacity of AA7A04-T6 SHS, eccentric-load tests were performed on eight specimens with a 5000-kN servo-control hydraulic compression equipment, as depicted in **Fig. 6**.

Fig. 6. Test setup.

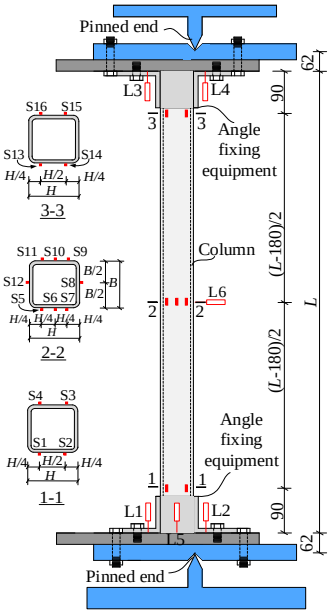

Fig. 7. Layout of strain gauges and LVDTs.

Knife-edge apparatus was mounted on both ends of the member to develop simply supported boundary conditions. The member underwent uniaxial eccentric compression, intending to bend about the *y*-axis (buckling axis). The centreline of member was shifted in the negative direction of the *x*-axis by a specified distance relative to the centreline of knife edge, ensuring that the eccentric load aligned with the specimen side surface exhibiting larger initial global geometric imperfections. Two sets of laser instruments were used during installation to calibrate specimens, projecting vertical and horizontal straight lines on their surfaces to coincide with the centreline of specimens. Angle fixing equipment was secured to both the upper and lower boundaries of the specimen for prevent column slippage during testing. Specimen end rotations were recorded by 4 linear variable differential transformers (LVDTs) placed at both the upper and lower bearing brackets. Additionally, sixteen strain gauges were mounted on each member, precisely positioned at cross-sections 90 mm separated from the member ends and the mid-span cross-sections utilizing the DH3816N Static Strain Acquisition Apparatus, as shown in **Fig. 7**. Note that all members were eccentrically loaded under a rate of 0.4 mm/min and the initial eccentricity (e_0) was calculated from Eq. (1),

$$e_0 = \frac{EI\left(\varepsilon_{\max} - \varepsilon_{\min}\right)}{NH} - \Delta - w_g \tag{1}$$

where $\varepsilon_{\max}$ and $\varepsilon_{\min}$ denote the strain readings at the strain gauges S8 and S12, respectively; I represents the inertia section moment, Δ is the lateral deflection at load N. Consistent with prior research [29], the

loading eccentricities were determined based on the strain responses observed at $N = 0.15N_{u,exp}$, where $N_{u,exp}$ signifies the experimental resistances of specimens under eccentric compression loading.

2.5 Tests results

Experimental results on AA7A04-T6 SHS members under eccentric loading were presented. The load-lateral deflection curves of all the members are depicted in **Fig. 8**, revealing a negative correlation between the $\overline{\lambda}_g$ and the resistance, and a positive correlation between the $\overline{\lambda}_g$ and the mid-span lateral deflection.

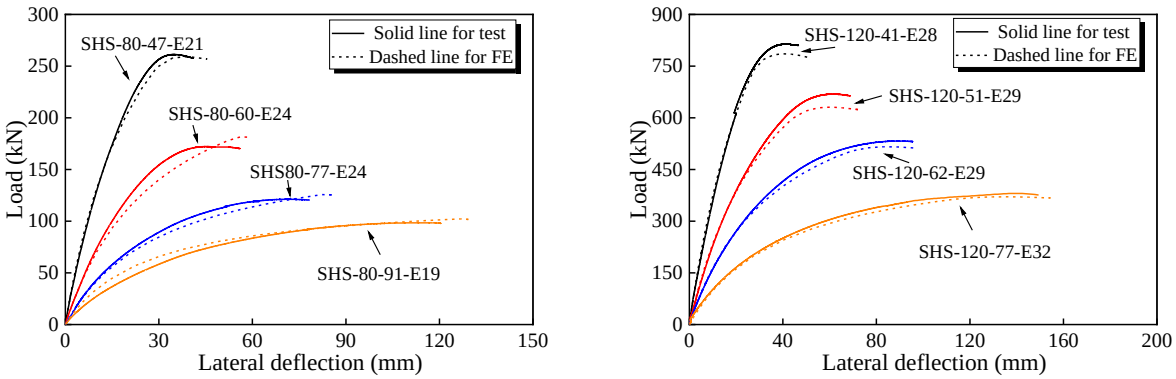

(a) SHS-80-5 (b) SHS-120-10

Fig. 8. Load-lateral deflection curves of specimens.

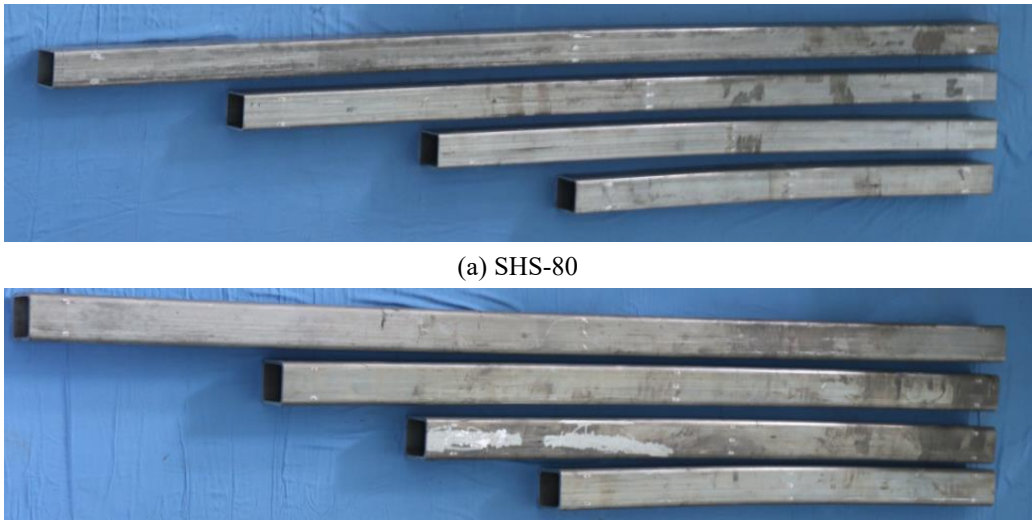

(a) SHS-80

(b) SHS-120

Fig. 9. Post-test deformed specimens.

Table 4. Summarized test/FE resistances of specimens

Specimen	$N_{u,exp}$ /kN	$N_{u,FE}$ /kN	$M_{u,exp}$ /kN·m	$N_{u,FE}$ /$N_{u,exp}$	Specimen	$N_{u,exp}$ /kN	$N_{u,FE}$ /kN	$M_{u,exp}$ /kN·m	$N_{u,FE}$ /$N_{u,exp}$
SHS-80-47-E21	261.26	259.25	5.56	0.992	SHS-120-41-E28	814.61	785.88	23.05	0.965
SHS-80-60-E24	172.15	181.46	4.06	1.054	SHS-120-51-E29	668.85	631.08	19.26	0.944
SHS-80-77-E24	121.22	125.69	2.92	1.037	SHS-120-62-E29	532.60	515.92	15.50	0.969
SHS-80-91-E19	98.40	102.25	1.89	1.039	SHS-120-77-E32	380.50	370.89	12.02	0.975
Mean									0.997
COV									0.039

All the specimens under eccentric loading failed by flexural buckling, with deformed specimens after tests shown in **Fig. 9**. Additionally, no instances of local buckling were observed during testing, which can be attributed to the non-slender characteristics of members. **Fig. 10** illustrates the deformed mode of two typical specimens under ultimate state. It is noteworthy that members with a larger slenderness ratio revealed significantly increased recovery capacity after flexural deformation. Key parameters of the failure loading ($N_{u,exp}$) and the moment ($M_{u,exp}= N_{u,exp} \cdot e_0$) at the member mid-span cross sections are summarized in **Table 4**, and the evaluation of recent design approaches was provided in later sections.

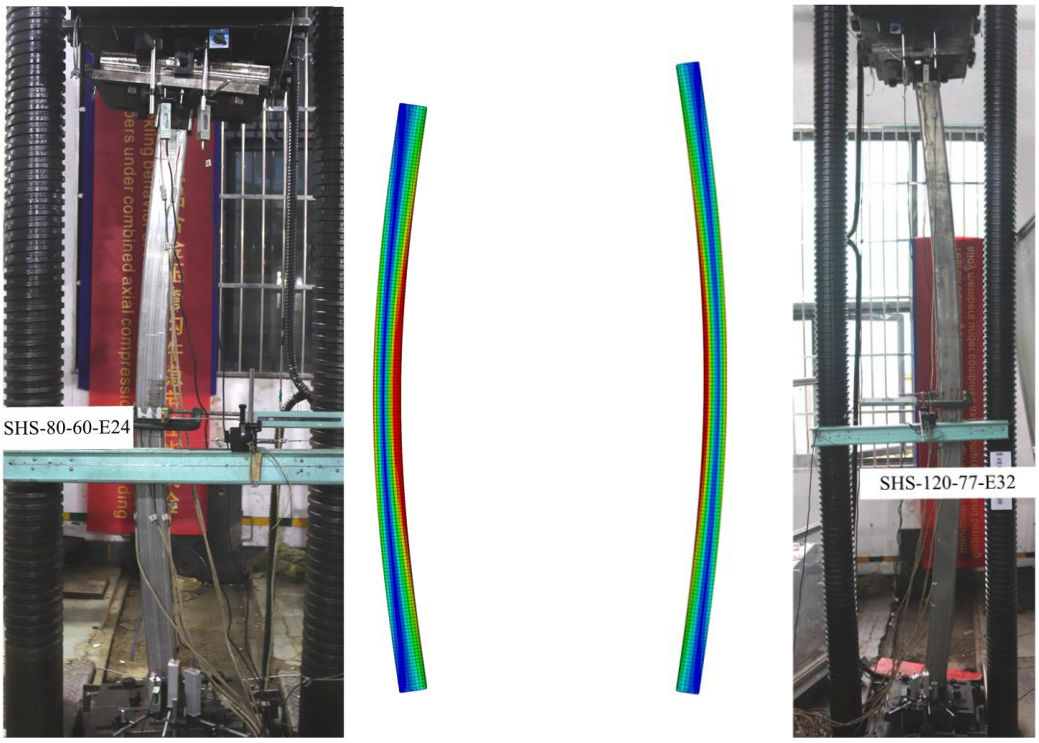

(a) SHS-80-60-E24 (b) SHS-120-77-E32

Fig. 10. Typical test versus FE failure modes.

3 Numerical study

Nonlinear numerical models were generated with FE software ABAQUS to expand the database of AA7A04-T6 SHS beam-columns under eccentric compression. These models served as valid cases to advance the investigation of flexural buckling properties for AA7A04-T6 SHS specimens, which cannot be easily obtained by a large number of physical tests.

3.1 Finite element modelling

Regarding the material model of AA7A04-T6, the true stress-strain datas, converted from the surveyed datas shown in **Fig. 4**, were incorporated into FE models. In the model, the 8-node linear brick element C3D8I was utilized, with a global element size of $2t \times 2t$ mm and 2 layers of elements in the thickness direction, which was consistent with prior numerical studies on AA SHS members [29]. Both ends of members were attached to reference point, RP1 and RP2, which were positioned away from longitudinal axis by e_0, and displaced from the column ends by 62 mm. Subsequently, RP1 was permitted to move along the longitudinal axis and rotate within the bending plane, while RP2 was restricted to rotation only within that plane to establish the pin-ended boundary conditions. Axial loads were introduced through RP1 using a displacement-controlled loading procedure to obtain complete load-mid-span lateral deflection curves. FE analysis was conducted using the static solver, considering material nonlinearities, geometric

nonlinearities, and initial imperfections. Note that the initial imperfections were considered by a half-sine curve, i.e., buckling analysis was conducted for each FE model to determine their global mode shape, and updated these FE model node coordinates via the "*imperfection" command, with the amplitude of the curve derived from the measurements recorded in **Table 3**.

3.2 Validation of FE models

The load-lateral deflection curves showed general consistency between FE models and tested specimens, as demonstrated in **Fig. 10** and **Table 3**. Meanwhile, **Fig. 8** illustrated that FE models effectively captured the flexural buckling failures compared to experimental counterparts. The eccentric compression resistances of all the FE models and test results are tabulated in **Table 4**, along with the average FE-to-test ratio and related coefficient of variation (COV) determined as 0.997 and 0.039, respectively. Consequently, the proposed models can be regarded as capable of replicating the experimental beam-column buckling behaviour, particularly the ultimate resistances, thus serving as a tool to assess the existing aluminium alloy beam-column design rules.

3.3 Parameter analysis

This part conducted a broad range of parameter analyses by using validated models to examine the buckling response of AA7A04-T6 extruded SHS members under eccentric compression. The parameters of non-dimensional slenderness ($\overline{\lambda}_g$), eccentricity ratio ($2e_0/B$) and the width-to-thickness ratio (b_f/t) of plate elements were taken into account. There were 512 AA7A04-T6 SHS FE models performed, covering two sets of thickness of 8 mm and 14 mm. Meanwhile, the width-to-thickness ratio (b_f/t) of plate elements ranged from 7.5 to 14.5, as illustrated in **Table 5**, with the $\overline{\lambda}_g$ ranging from 0.30 to 3.4, also including the eccentricity ratio ($2e_0/B$) of 0, 0.1, 0.3, 0.5, 1, 2, 4, and 15.

Table 5. Dimensions of specimens' cross sections in parametric investigations (unit: mm)

b_f/t	$B\times H\times t$	b_f/t	$B\times H\times t$
8.5	84×84×8	7.5	133×133×14
10.5	100×100×8	9.5	161×161×14
12.5	116×116×8	11.5	189×189×14
14.5	132×132×8	13.5	217×217×14

All the FE models were confined to the Class 2 and Class 3 domains set out in European provisions [21], which complied with the non-slender cross sections specified in Chinese provisions [22]. The mean mechanical characteristics of AA7A04-T6 detailed in **Table 2** were incorporated into the models, specifically determined as E = 74.57 Gpa, $\sigma_{0.2}$ = 544.3 Mpa, σ_u = 621.5 Mpa and n = 28.2. In all FE models, an initial global geometric imperfection was included and set to L_e/1000 for safety purposes.

4 Evaluation of codified design approaches and a new modification strategy

To evaluate the suitability of design approaches set out in European provisions [21], Chinese standard [22] and American code [23] to AA7A04-T6 SHS beam-columns, the test and FE findings were contrasted with the resistances predicted from the codified design approaches. The experimental and FE resistances are denoted as $N_{u,FE/test}$ and $M_{u,FE/test}$, respectively, while the predicted resistances are represented as $N_{Rd,EC9}$, $N_{Rd,GB}$, $N_{Rd,AADM}$ representing the European, Chinese and American provisions. The unity for the resistance factor and measured proof strengths were used to calculate the predicted resistances described in the following. Noted that this paper focuses on Class 1-3 cross-sections, and does not consider content related to effective cross-sections and failures due to local buckling.

4.1 European provision (EN 1999-1-1:2007)

The classification of cross-sections is fundamental concept in European provision [21], which considers 4 classes of cross-sections. Based on this concept, all cross-sections are valid for Class 1~3, while effective thickness must be considered for Class 4 when calculating member resistances. In European standard, a nonlinear interactive equation is employed for beam-columns, as denoted in Eq. (2),

$$\left(\frac{N_{\mathrm{Ed,EC9}}}{N_{\mathrm{Rd,EC9}}}\right)^{0.8}+\frac{1}{\omega_0}\left[\left(\frac{M_{\mathrm{Ed,EC9}}}{M_{\mathrm{Rd,EC9}}}\right)^{1.7}\right]^{0.6}\le 1.0 \tag{2}$$

where ω_0 is the factor for the section with localized weld, and ω_0 = 1.0 in this paper; N_{Ed} represents the design value to axial force, M_{Ed} represents the design value to moment. $N_{\mathrm{Rd,EC9}}$ is the column resistance under axial compression, which is given by $\omega_x\chi\sigma_{0.2}A_g/\gamma_{\mathrm{R,EC9}}$, hereinto ω_x has the same meaning as ω_0 and equal to 1.0, $\gamma_{\mathrm{R,EC9}}$ represents the resistance factor and defined as 1.1. χ represents the reduction factor and is determined using $\chi=(\phi+\sqrt{\phi^2-\bar{\lambda}_g^2})^{-1}$, where ϕ is calculated by ϕ = 0.5(1+α_i($\bar{\lambda}_g$ - $\bar{\lambda}_0$)+$\bar{\lambda}_g$), hereinto α_i is the imperfection factor and defined as 0.2 for AA in T6 temper, $\bar{\lambda}_0$ is the limit of the horizontal plateau of buckling curve and defined as 0.1. The pure bending resistance $M_{\mathrm{Rd,EC9}}$ is given by $\alpha\sigma_{0.2}W_{\mathrm{el}}/\gamma_{\mathrm{R,EC9}}$, in which α represents the shape factors and is calculated by Eq. (3),

$$\alpha=\begin{cases}5-(3.89+0.0019n)\Big/\left(W_{\mathrm{pl}}/W_{\mathrm{el}}\right)^{(0.27+0.0014n)} & \text{for Class 1}\\ W_{\mathrm{pl}}/W_{\mathrm{el}} & \text{for Class 2}\\ 1 & \text{for Class 3}\\ W_{\mathrm{eff}}/W_{\mathrm{el}} & \text{for Class 4}\end{cases} \tag{3}$$

where W_{el} represents the elastic section modulus, W_{pl} represents the plastic section modulus, W_{eff} represents the effective elastic section modulus.

4.2 Chinese provision (GB 50429-2007)

When evaluating the stability of AA beam-columns, the Chinese standard [22] considers a correlation between axial force and moment described in Eq. (4),

$$\frac{N_{\mathrm{Ed,GB}}}{N_{\mathrm{Rd,GB}}}+\frac{\beta_{\mathrm{mx}}M_{\mathrm{Ed,GB}}}{M_{\mathrm{Rd,GB}}}\le 1.0 \tag{4}$$

where $N_{\mathrm{Rd,GB}}=\chi\sigma_{0.2}A_g/\gamma_{\mathrm{R,GB}}$ for non-slender cross-section members, which is closely resemble that in EN 1999-1-1:2007 [21], while $\bar{\lambda}_0$ is set to 0.15 when calculating χ, leading to a more conservative resistances to the axially compressed columns. $M_{\mathrm{Rd,GB}}=\left(1-\eta_1 N_{\mathrm{Ed}}/N'_{\mathrm{E}}\right)\gamma_x\sigma_{0.2}W_{\mathrm{el}}\big/\gamma_{\mathrm{R,GB}}$, hereinto η_1 is the reduction coefficient and set to 0.75, γ_x is the plastic development factor and taken as 1.0 for SHS, N'_{E} is the nominal Euler load and calculated as $\pi^2EA/(1.2\lambda^2)$. β_{mx} and $\gamma_{\mathrm{R,GB}}$ are set to 1.0 and 1.2, respectively.

4.3 American provision (AADM-2020)

AADM-2020 [23] checks the member resistances by all possible failure modes and their corresponding minimum values to be the allowable strength. Following this approach, the limit state is divided into flexural buckling, local buckling, and flexural-local buckling for axially compressed members, while it involves member yielding, rupture, and local buckling for bending members. Subsequently, the allowable strength of compression and bending can be calculated based on the member's limit state. For SHS members under combined axial forces and bending moments, AADM-2020 [23] employs linear expressions to describe the interaction between axial forces and moments, as outlined by Eq. (5),

$$\left|\frac{N_{\mathrm{Ed,AA}}}{N_{\mathrm{Rd,AA}}}+\frac{M_{\mathrm{Ed,AA}}}{M_{\mathrm{Rd,AA}}}\right|\le 1.0 \tag{5}$$

where $N_{Rd,AA}$ and $M_{Rd,AA}$ represent the resistances of the axially compressed members and pure bending members, respectively, and can be obtained using Eqs. (6) and (7),

$$N_{Rd,AA} = \phi_c \cdot \min\left(\sigma_c A_g,\ \sum_{i=1}^{n}\sigma_{ci}A_i + \sigma_{0.2}\left(A_g - \sum_{i=1}^{n}A_i\right),\ \left(0.85\pi^2 E/\lambda^2\right)^{1/3}\sigma_e^{2/3}A_g\right) \tag{6}$$

$$M_{Rd,AA} = \phi_c \cdot \min\left(W_{pl}\sigma_{cy},\ 1.5Z_t\sigma_{ty},\ 1.5Z_c\sigma_{cy},\ W_{pl}\sigma_{tu}/\gamma_t,\ \sigma_{ci}I_f/c_{cf} + \sigma_{bi}I_w/c_{cw}\right) \tag{7}$$

where ϕ_c is set to 0.90, σ_c represents compress critical stress at the member level, which can be expressed as Eq. (8),

$$\sigma_c = \begin{cases} \sigma_{0.2} & \text{for } \lambda \le C_b \\ (B_c - D_c\lambda)[0.85 + 0.15(C_c - \lambda)/(C_c - C_b)] & \text{for } C_b < \lambda \le C_c \\ 0.85\pi^2 E/\lambda^2 & \text{for } \lambda > C_c \end{cases} \tag{8}$$

where $C_b = (B_c\text{-}\sigma_{0.2})/D_c$; B_c, C_c and D_c represent the flexure coefficients. Additionally, σ_{ci} signifies the local buckling strength of plate; σ_e represents the minimum elastic local buckling strength and given by $\pi^2E/(1.6b/t)^2$; σ_{bi} signifies the flexural compressive stress of plate, while σ_{cy} and σ_{ty} are the compressive and tension 2% proof stress, respectively; Z_t and Z_c indicate the section modulus about tension and compression sides of the neutral axis, respectively; σ_{tu} represents the tension ultimate stress; γ_t represents the tensile parameter; I_f and I_w denote the moments of inertia of the member height and width about the neutral axis of the profile, respectively; c_{cf} and c_{cw} represent the distances off the outermost compression fibre of the member height and width to the neutral axis, respectively.

4.4 Evaluation of the codified and modified design approaches

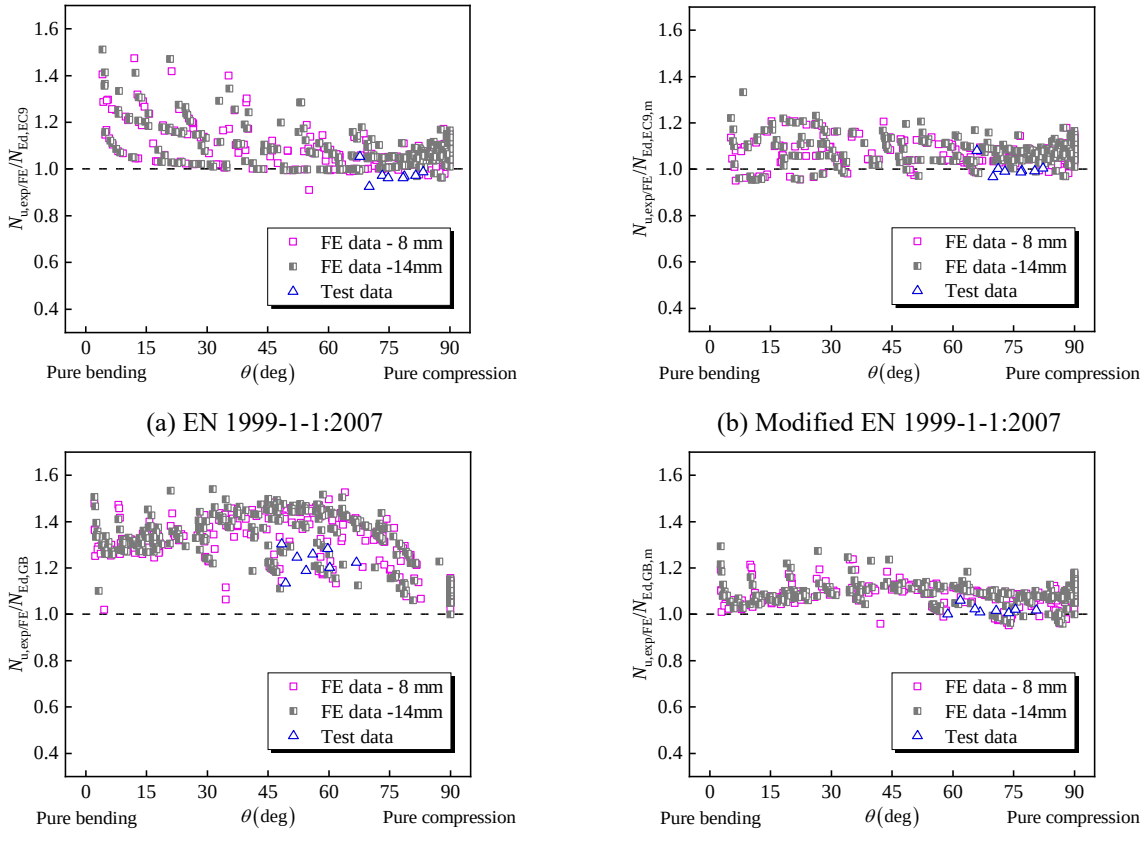

(a) EN 1999-1-1:2007

(b) Modified EN 1999-1-1:2007

(c) GB 50429-2007

(d) Modified GB 50429-2007

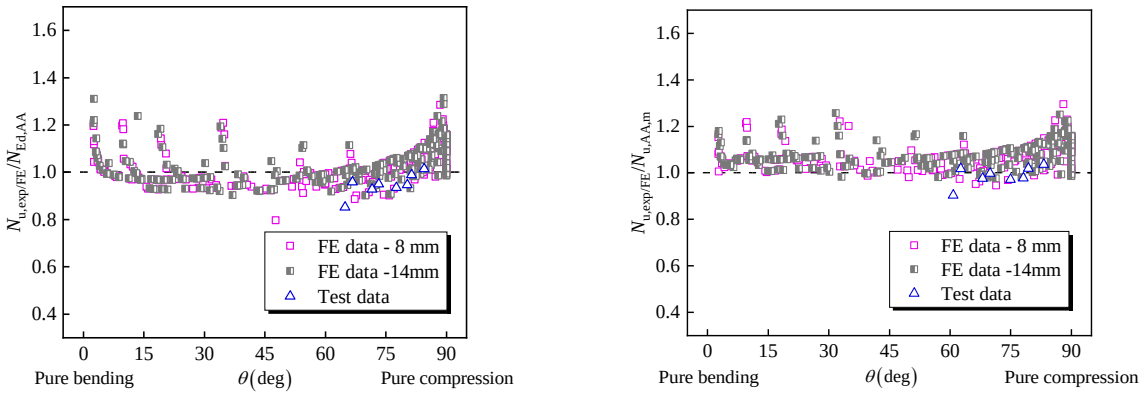

(e) AADM-2020 (f) Modified AADM-2020

Fig. 11. Assessment of test/FE findings using codified and modified design approaches.

The accuracy of the codified design approaches on the stability forecasts of AA7A04-T6 SHS beam-columns was summarised and evaluated, as depicted in **Fig. 11**, in which $N_{u,exp/FE}/N_{Ed,EC9}$, $N_{u,exp/FE}/N_{Ed,GB}$ and $N_{u,exp/FE}/N_{Ed,AA}$ represent the resistance ratios of experimental and FE findings to codified predictions according to the European [21] , Chinese [22] and American provisions [23] respectively. These ratios were calculated based on the standard theoretical value corresponding to θ, where θ is the angle parameter given by Eq. (9) and defined in **Fig. 12**. It's worth noting that $\theta = 0°$ corresponds to pure moment and $\theta = 90°$ corresponds to axial force.

$$\theta = \tan^{-1}\left[\left(N_{Ed}/N_{Rd}\right)/\left(M_{Ed}/M_{Rd}\right)\right] \tag{9}$$

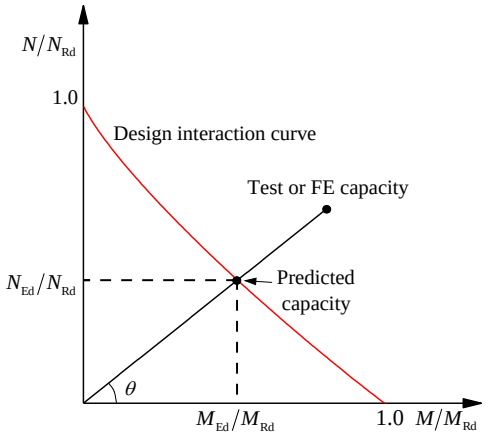

Fig. 12. Definition of θ on compression–bending interaction curve.

The average values of $N_{u,exp/FE}/N_{Ed,EC9}$, $N_{u,exp/FE}/N_{Ed,GB}$ and $N_{u,exp/FE}/N_{Ed,AA}$ and corresponding COVs are detailed in **Table 7**. The mean ratio $N_{u,exp/FE}/N_{Ed,AA}$ predicted by the AADM-2020 [23] was 1.040, with a corresponding COV of 0.084, indicating relatively accurate predictions compared to the other two standards. However, many data points lied on unsafe side in **Fig. 11 (e)**. Meanwhile, it exhibited an overly conservative bias and notable inaccuracies in estimating the pure bending and axial compression, which was consistent with the results calculated by the other two standards. These deviations were attributed to the neglecting of the strain hardening and plate interactions, coupled with inaccurate curvilinear form for combined compression and bending, leading to the underestimation of end points. Besides, the average ratio $N_{u,exp/FE}/N_{Ed,GB}$ and its COV in accordance with the GB 50429-2007 [22] were 1.304 and 0.094, respectively, demonstrating that the strength forecasts were excessively conservative and widely dispersed, particularly when the bending effect was in dominant state, resulting in a general underestimation of resistances.

Table 7. Comparisons of test/FE findings with forecasted resistances through several design approaches

Ratio	$N_{u,exp/FE}$ /$N_{Ed,EC9}$	$N_{u,exp/FE}$ /$N_{Ed,GB}$	$N_{u,exp/FE}$ /$N_{Ed,AA}$	$N_{u,exp/FE}$ /$N_{Ed,EC9,M}$	$N_{u,exp/FE}$ /$N_{Ed,GB,M}$	$N_{u,exp/FE}$ /$N_{Ed,AA,M}$
Mean	1.086	1.304	1.040	1.074	1.081	1.078
COV	0.083	0.094	0.084	0.051	0.046	0.056

Previous research [34] argued that the interaction between compression and flexure was chiefly influenced by $\overline{\lambda}_g$ and $N_{u,exp/FE}/N_{Rd}$. Based on the design approaches in EN 1993-1-1 [35], they suggested a interaction buckling factor (k) suitable for stainless steel SHS members, as shown in Eqs. (10) and (11). Given the inapplicability of AA7A04-T6 columns under eccentric loading to current standards, an improved method for designing the aluminium alloy beam-columns within the framework of existing standards was suggested under the concentration of the interaction buckling factors (k).

$$\frac{N_{Ed}}{N_{Rd}}+k_{G\&K}\frac{M_{Ed}}{M_{Rd}}\le 1.0 \tag{10}$$

$$k_{G\&K}=0.9+3.5\left(\frac{N_{Ed}}{N_{Rd}}\right)^{1.8}\left(\overline{\lambda}_g-0.5\right)\le 0.9+1.75\left(\frac{N_{Ed}}{N_{Rd}}\right)^{1.8} \tag{11}$$

Specifically, the constant terms in Eq. (11) were numerically fitted using the results of Eq. (12), and subsequently adjusted for safety considerations. This procedure yielded the corresponding AA7A04-T6 SHS beam-column interaction buckling coefficients for the three standards, as given by Eqs. (13) ~ (15). Finally, the interaction buckling factor was added in the three standards, as shown in Eqs. (16) ~ (18).

$$k=\begin{cases}\left(1-\dfrac{N_{Ed}}{N_{Rd}}\right)\dfrac{M_{Rd}}{M_{Ed}} & \text{for GB 50429-2007 or AADM-2020}\\ \left(1-\left(\dfrac{N_{Ed}}{N_{Rd}}\right)^{0.8}\right)\left(\dfrac{M_{Rd}}{M_{Ed}}\right)^{1.02} & \text{for EN 1999-1-1:2007}\end{cases} \tag{12}$$

$$k_{EC9}=0.8+0.5\left(\frac{N_{Ed}}{N_{Rd}}\right)^{0.8}\left(\overline{\lambda}_g-0.5\right)\le 1+0.2\left(\frac{N_{Ed}}{N_{Rd}}\right) \tag{13}$$

$$k_{GB}=0.8-0.19\left(\frac{N_{Ed}}{N_{Rd}}\right)^{2}\left(\overline{\lambda}_g-0.17\right)\le 1.5-1.3\left(\frac{N_{Ed}}{N_{Rd}}\right) \tag{14}$$

$$k_{AA}=0.9+0.2\left(\frac{N_{Ed}}{N_{Rd}}\right)^{0.5}\left(\overline{\lambda}_g+1\right)\le 1+0.25\left(\frac{N_{Ed}}{N_{Rd}}\right)^{0.5} \tag{15}$$

$$\left(\frac{N_{Ed,EC9,M}}{\chi_{min}\omega_x N_{Rd,EC9}}\right)^{0.8}+\frac{k_{EC9}}{\omega_0}\left[\left(\frac{M_{Ed,EC9,M}}{M_{Rd,EC9}}\right)^{1.7}\right]^{0.6}\le 1.0 \tag{16}$$

$$\frac{N_{Ed,GB,M}}{N_{Rd,GB}}+\frac{k_{GB}\beta_{mx}M_{Ed,GB,M}}{M_{Rd,GB}}\le 1.0 \tag{17}$$

$$\left|\frac{N_{Ed,AA,M}}{N_{Rd,AA}}+\frac{k_{AA}M_{Ed,AA,M}}{M_{Rd,AA}}\right|\le 1.0 \tag{18}$$

The comparison of test/FE findings to the calculated carrying capacity with the modified strategy is presented against the angle parameter, as displayed in **Fig. 11** and **Table 7**. It was demonstrated that the modified methods exhibited better accuracy and consistency for the combined force and moment carrying capacity of the SHS members, especially for the members under the dominant of compression or bending.

Among these methods, the modified Chinese standard [22] showed an excellent improvement, with the average ratio reduced by about 22% and COV by about 48%. Meanwhile, most forecasted results were moved to the safe range when using the modified approach for the AA-2020, with a slight increase of conservatism but reduced scattered predictions. Therefore, the revised approach provided greater effectiveness in forecasting the flexural buckling resistances for AA7A04-T6 members relative to the codified design approaches.

5 Conclusions

This paper provides an extensive experimental and FE analysis focused on examining the stability for AA7A04-T6 SHS beam-columns. The key conclusions include:

(1) The flexural buckling failure mode was observed for eight AA7A04-T6 SHS columns with Class 2 and Class 3 cross-sections under eccentric compression, accompanied by significant lateral deflections.

(2) The design methods specified in EN 1999-1-1:2007, GB 50429-2007, and AADM-2020 consistently and conservatively predicted the resistances of SHS beam-columns by approximately 9%, 30%, and 4% lower, respectively.

(3) Three codified design approaches exhibited identifiable shortcomings in terms of the high level of conservative and dispersed results, which was primarily due to unreasonable interaction curve patterns and inaccurate compression and bending end points.

(4) A new revised approach, derived from modified interaction buckling factors taking into account non-dimensional slenderness and axial force resistances, was suggested. It showed better accuracy and consistency than codified design approaches in stability forecasts of AA7A04-T6 SHS beam-columns.

Funding Statement

This work was financially supported by the National Natural Science Foundation of China (No. 52108154), the Fundamental Research Funds for the Central Universities (No. JZ2023HGTB0258), the Guangxi Science and Technology Major Program (No. AA23073019) and the Open Foundation of State Key Laboratory of Featured Metal Materials and Life-cycle Safety for Composite Structures (No. MMCS2023OF13).

CRediT authorship contribution statement

Beibei Li: Conceptualization, Funding acquisition, Writing – original draft. **Pengcheng He**: Methodology, Writing – review& editing. **Jingfeng Wang**: Investigation. **Yuanqing Wang**: Supervision.

Conflicts of Interest

The authors declare that they have no conflicts of interest to report regarding the present study.

References

[1] Georgantzia E, Gkantou M, Kamaris G. Aluminium alloys as structural material: A review of research. Engineering Structures 2021; 227: 111372. https://doi.org/10.1016/j.engstruct.2020.111372.

[2] You XH, Xing ZQ, Jiang SW, Zhu Y, Lin YH, Qiu HS, Nie RJ, Yang JH, Hui D, Chen W, Chen Y. A review of research on aluminum alloy materials in structural engineering. Developments in the built environment 2024; 17: 100319. https://doi.org/10.1016/j.dibe.2023.100319.

[3] Liu HB, Ying JJ, Chen ZH, Ma CJ, Qian SQ, Ouyang YW, Liu XW. Research status of mechanical properties of aluminum alloy grid structure. Structures 2024; 61: 105967. https://doi.org/10.1016/j.istruc.2024.105967.

[4] Su MN, Young B, Gardner L. Testing and design of aluminium alloy cross-sections in compression. Journal of Structural Engineering 2014; 140(9): 04014047. https://doi.org/10.1061/(ASCE)ST.1943-541X.0000972.

[5] Wang ZX, Wang YQ, Sojeong J, Ouyang YW. Experimental investigation and parametric analysis on overall buckling behavior of large-section aluminum alloy columns under axial compression. Thin-Walled Structures

2018; 122: 585-596. https://doi.org/10.1016/j.tws.2017.11.003.
[6] Zhang Y, Wang YQ, Wang ZX, Bu YD, Fan SG, Zheng BF. Experimental investigation and numerical analysis of pin-ended extruded aluminium alloy unequal angle columns. Engineering Structures 2020; 215: 110694. https://doi.org/10.1016/j.engstruct.2020.110694.
[7] Adeoti GO, Fan F, Wang YJ, Zhai XM. Stability of 6082-T6 aluminium alloy columns with H-section and rectangular hollow sections. Thin-Walled Structures 2015; 89: 1-16. https://doi.org/10.1016/j.tws.2014.12.002.
[8] Wang YJ, Fan F, Lin SB. Experimental investigation on the stability of aluminium alloy 6082 circular tubes in axial compression. Thin-Walled Structures 2015; 89: 55-66. https://doi.org/10.1016/j.tws.2014.11.017.
[9] Moen LA, Hopperstad OS, Langseth M. Rotational capacity of aluminum beams under moment gradient. I: Experiments. Journal of Structural Engineering 1999; 125(8): 910-920. https://doi.org/10.1061/(ASCE)0733-9445(1999)125:8(910).
[10] Zhu JH, Young B. Experimental investigation of aluminum alloy thin-walled tubular members in combined compression and bending. Journal of Structural Engineering 2006; 132(12): 1955-1966. https://doi.org/10.1061/(ASCE)0733-9445(2006)132:12(1955).
[11] Su MN, Young B, Gardner L. The continuous strength method for the design of aluminium alloy structural elements. Engineering Structures 2016; 122: 338-348. https://doi.org/10.1016/j.engstruct.2016.04.040.
[12] Kim Y, Peköz T. Numerical Slenderness Approach for design of complex aluminum extrusions subjected to flexural loading. Thin-Walled Structures 2018; 127: 62-75. https://doi.org/10.1016/j.tws.2018.01.029.
[13] Feng R, Yang T, Chen ZM, Roy K, Chen BS, Lim JBP. Finite-element analysis and design of aluminum alloy RHSs and SHSs with through-openings in bending. Steel and Composite Structures 2023; 46(3): 353-366. https://doi.org/10.12989/scs.2023.46.3.353.
[14] Zhu JH, Young B. Aluminum alloy circular hollow section beam-columns. Thin-Walled Structures 2006; 44: 131-140. https://doi.org/10.1016/j.tws.2006.02.006.
[15] Du P, Liu HB, Li XL, Chen ZH, Ying JJ. Stability properties of 6061-T6 aluminum alloy members with double-layer H-type sections under eccentric compression loads. Engineering Structures 2024; 305: 117687. https://doi.org/10.1016/j.engstruct.2024.117687.
[16] Zhao YZ, Zhai XM, Sun LJ. Test and design method for the buckling behaviors of 6082-T6 aluminum alloy columns with box-type and L-type sections under eccentric compression. Thin-Walled Structures 2016; 100: 62-80. https://doi.org/10.1016/j.tws.2015.12.010.
[17] Zhao YZ, Zhai XM, Wang JH. Buckling behaviors and ultimate strengths of 6082-T6 aluminum alloy columns under eccentric compression - Part I: Experiments and finite element modeling. Thin-Walled Structures 2019; 143: 106207. https://doi.org/10.1016/j.tws.2019.106207.
[18] Kong WY, Yang H, Zhou L, Xing ZQ, Chen Y. Study on stability of H-type section aluminum alloy perforated members under axial compression and eccentric compression around weak axis. Thin-Walled Structures 2024; 195: 111533. https://doi.org/10.1016/j.tws.2023.111533.
[19] Zhi XH, Wang YQ, Zhang Y, Li BB, Ouyang YW. Study of local buckling performance of 7075-T6 high-strength aluminium alloy H-section stub columns. Thin-Walled Structures 2022; 180: 109925. https://doi.org/10.1016/j.tws.2022.109925.
[20] Georgantzia E, Gkantou M, Kamaris GS, Kansara KD. Ultimate response and plastic design of aluminium alloy continuous beams. Structures 2022; 39: 175-193. https://doi.org/10.1016/j.istruc.2022.03.015.
[21] EN 1999-1-1:2007, Eurocode 9: Design of aluminium structures. Part 1-1: General structural rules-General structural rules and rules for buildings. Brussels: European Committee for Standarization, 2007.
[22] GB 50429-2007, Code for design of aluminium structures. Beijing: China Planning Press, 2007. (in Chinese)
[23] ADM-2020, Aluminum design manual. Washington DC: The Aluminum Association, 2020.
[24] Wan J, Zhu Y, Zhang Y, Zhao H. Strain rate effect and dynamic constitutive model of 7A04-T6 high-strength aluminium alloy. Structures 2023; 53: 1250-1266. https://doi.org/10.1016/j.istruc.2023.05.013.
[25] Quan H, Alderliesten RC. The relation between fatigue crack growth rate and plastic energy dissipation in 7075-T6. Engineering Fracture Mechanics 2021; 252: 107765. https://doi.org/10.1016/j.engfracmech.2021.107765.
[26] Wang YQ, Wang ZX. Experimental investigation and FE analysis on constitutive relationship of high strength aluminum alloy under cyclic loading. Advances in Materials Science and Engineering 2016; 1-16. https://doi.org/10.1155/2016/2941874.
[27] Yun X, Wang ZX, Gardner L. Full-range stress-strain curves for aluminium alloys. Journal of Structural Engineering 2021; 147(6): 04021060. https://doi.org/10.1061/(ASCE)ST.1943-541X.0002999.
[28] Rong B, Guo Y, Li ZY. Study on the stability behavior of 7A04-T6 aluminum alloy square and rectangular hollow section columns under axial compression. Journal of Building Engineering 2022; 45: 103652.

https://doi.org/10.1016/j.jobe.2021.103652.
[29] Li BB, Wang YQ, Zhang Y, Meng X, Yuan HX, Zhi XH. Flexural buckling of extruded high-strength aluminium alloy SHS columns. Thin-Walled Structures 2022; 179: 109717. https://doi.org/10.1016/j.tws.2022.109717.
[30] Li BB, Wang YQ, Zhang Y, Zhi XH, Lin S. Flexural buckling of high-strength aluminium alloy CHS columns. Structures 2022; 43: 223-233. https://doi.org/10.1016/j.istruc.2022.06.036.
[31] Yuan L, Zhang QL, Ouyang YW. Experimental investigation and design method of the flexural buckli-ng resistance of high-strength aluminum alloy H-columns. Structures 2022; 35: 1339-1349. https://doi.org/10.1016/j.istruc.2021.11.013.
[32] Hu YW, Rong B, Zhang RY, Zhang YC, Zhang S. Study of buckling behaviour for 7A04-T6 alumin-um alloy rectangular hollow columns. Thin-Walled Structures 2021; 169: 108410. https://doi.org/10.1016/j.tws.2021.108410.
[33] Rong B, Zhang YC, Zhang S, Li ZY. Experiment and numerical investigation on the buckling behavior of 7A04-T6 aluminum alloy columns under eccentric load. Journal of Building Engineering 2022; 45: 103625. https://doi.org/10.1016/j.jobe.2021.103625.
[34] Greiner R, Kettler M. Interaction of bending and axial compression of stainless steel members. Journal of Constructional Steel Research 2008; 64(11): 1217-1224. https://doi.org/10.1016/j.jcsr.2008.05.008.
[35] EN 1993-1-1, Eurocode 3: design of steel structures - Part 1. 1: general rules and rules for buildings. Brussels: European Committee for Standardization, 2005.